

In-gap states and strain-tuned band convergence in layered structure trivalent iridate $\text{K}_{0.75}\text{Na}_{0.25}\text{IrO}_2$

Xujia Gong,¹ Carmine Autieri,² Huanfu Zhou,³ Jiafeng Ma,¹ Xin Tang,³ Xiaojun Zheng,¹

Xing Ming,^{1*}

1. College of Science, Guilin University of Technology, Guilin 541004, People's Republic of China

2. International Research Centre Magtop, Polish Academy of Sciences, Aleja Lotników 32/46, PL-02668 Warsaw

3. Key Lab of New Processing Technology for Nonferrous Metal & Materials, Ministry of Education, School of Materials Science and Engineering, Guilin University of Technology, Guilin 541004, China.

ABSTRACT

Iridium oxides (iridates) provide a good platform to study the delicate interplay between spin-orbit coupling (SOC) interactions, electron correlation effects, Hund's coupling and lattice degree of freedom. However, overwhelming investigations primarily focus on tetravalent (Ir^{4+} , $5d^5$) and pentavalent (Ir^{5+} , $5d^4$) iridates, far less attention has been paid to iridates with other valence states. Here, we pay our attention to a less-explored trivalent (Ir^{3+} , $5d^6$) iridates, $\text{K}_{0.75}\text{Na}_{0.25}\text{IrO}_2$, crystalizing in a triangular lattice with edge-sharing IrO_6 octahedra and alkali metal ions intercalated $[\text{IrO}_2]^-$ layers. We theoretically determine the preferred occupied positions of the alkali metal ions from energetic viewpoints and reproduce the experimentally observed semiconducting behavior and nonmagnetic (NM) properties. The SOC interactions play a critical role in the band dispersion, resulting in NM $J_{\text{eff}} = 0$ states. More intriguingly, our electronic structure not only uncovers the presence of in-gap states and explains the abnormal low activation energy in $\text{K}_{0.75}\text{Na}_{0.25}\text{IrO}_2$, but also predicts the band edge can be effectively modulated by mechanical strain. Especially, the in-gap states feature with enhanced band-convergence characteristics by 6% compressive strain, which will greatly enhance the electrical conductivity of $\text{K}_{0.75}\text{Na}_{0.25}\text{IrO}_2$. Present work sheds new lights on the unconventional electronic structures of the trivalent iridates, indicating its promising application as nanoelectronic and thermoelectric material.

*Email: mingxing@glut.edu.cn

I. INTRODUCTION

Due to the intricate interplay between electron correlation, Hund exchange coupling, spin-orbit coupling (SOC) and crystal field splitting, iridium oxides (iridates) exhibit novel phenomena and intriguing properties [1-8]. Normally, the d orbitals are split into three-fold degenerate t_{2g} and two-fold degenerate e_g states by the octahedral crystal field. Interestingly, attributed to large octahedral crystal-field splitting and strong SOC interactions in iridates, the triply degenerate t_{2g} states will further evolve into $j_{\text{eff}} = 3/2$ quartet and $j_{\text{eff}} = 1/2$ doublet states [9]. The j_{eff} state has been proposed as a common ingredient in iridates, arousing researchers' passion to explore the interplay between electron correlations and SOC interactions. Depending on the relative strength of Coulomb repulsion and SOC interactions, exotic phases have been revealed in iridates [1,4], such as spin-orbit coupled Mott insulators [9,10], Weyl semimetals [11,12], topological insulators [4,13], giant magnetic anisotropy [14,15], superconductors [16-19], spin liquids and spin ices [20,21]

Furthermore, the effective electron correlations and SOC interactions increase with the decreasing geometry connectivity (the connection manner between the polyhedral units) in iridates [5-7]. The crucial roles played by the lattice degree of freedom and geometric connectivity in iridates have renewed growing interests in iridates. The IrO_6 octahedra often arrange in a mixed corner- and edge-sharing network. The structural dimensionality and the stacking manner of the IrO_6 octahedra can be used to manipulate the electronic structure of iridates [6,22], such as dimensionality-driven metal-insulator transition (MIT) in the Ruddlesden-Popper series $\text{Sr}_{n+1}\text{Ir}_n\text{O}_{3n+1}$ compound [5,23], novel $j_{\text{eff}} = 1/2$ Mott insulating state in quasi-two-dimensional Sr_2IrO_4 [9,10], and semimetallic SrIrO_3 with unusually narrow bandwidths [24]. Overwhelming investigations have focused on the tetravalent and pentavalent iridates with $5d^5$ (Ir^{4+}) and $5d^4$ (Ir^{5+}) electronic configurations, far less attention have been paid to iridates with other valence states and electronic configurations.

Recently, an unprecedented trivalent iridate $\text{K}_{0.75}\text{Na}_{0.25}\text{IrO}_2$ was synthesized by Weber *et al.*, where the Ir^{3+} ions adopting a $5d^6$ electron configuration [25]. As shown in **Figure 1**, $\text{K}_{0.75}\text{Na}_{0.25}\text{IrO}_2$ crystallizes in a triangular lattice with $P6_3/\text{mmc}$ space group. The edge-sharing IrO_6 octahedra form two-dimensional $[\text{IrO}_2]^-$ layers. The alkali metal ions act as intercalated ions, occupying two types of interlayer sites: A ($1/3, 2/3, 1/4$) and B ($0, 0, 1/4$), respectively. Experiments indicate that the Na ions almost only occupy the interlayer positions A, whereas two third (one third) of the K ions occupy the interlayer positions A (B), concomitant with 25% (75%) vacancies in the positions A (B).

The uncommon trivalent iridium ions and the triangular layered structure of $\text{K}_{0.75}\text{Na}_{0.25}\text{IrO}_2$ offer a promising platform to explore the interplay between electron correlations, SOC interactions, and lattice degree of freedom. $\text{K}_{0.75}\text{Na}_{0.25}\text{IrO}_2$ shows nonmagnetic (NM) characteristics and semiconducting behavior by magnetic property and electrical resistivity measurements. However, experimentally determined activation energy (85.7 meV) is very low for this semiconductor. Although elementary electronic structure has been attached in the originally experimental work, the authors only considered one composition of the alkali metal ions by completely neglecting the Na ions, where the interlayer positions only occupied by K ions. Therefore, the electronic structure corresponds to KIrO_2 , showing a big band gap of 0.973 eV, and the abnormal activation energy remains to be clarified [25].

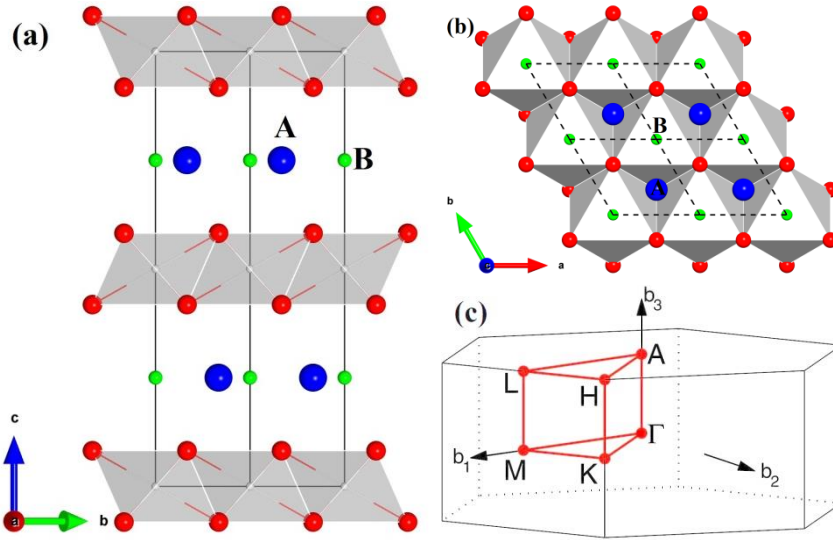


Figure 1 (a) Side view and (b) top view of the crystal structure of $\text{K}_{0.75}\text{Na}_{0.25}\text{IrO}_2$ drawn with VESTA [26], and (c) corresponding k -path of the Brillouin zone generated with AFLOW [27,28]. The $[\text{IrO}_2]^-$ layers consist of edge-sharing IrO_6 octahedra on a triangular lattice (the dashed line denotes a unit cell). Two types of interlayer sites are occupied by the alkali metal ions, where the big/small balls denote the positions A/B facing hallow/face of the octahedra.

In the present work, we not only consider the interlayer positions fully occupied by one type of alkali metal ions, but also consider more complexed occupancies of the mixed alkali metal ions. Especially, in order to capture the real occupancy of the alkali metal ions and inspect the intrinsic characteristics of the title compound of $\text{K}_{0.75}\text{Na}_{0.25}\text{IrO}_2$, we have built supercell to consider the distribution of alkali metal ions and vacancies in the interlayer space. These settings of the structure

model are much more consistent with the real composition of $\text{K}_{0.75}\text{Na}_{0.25}\text{IrO}_2$. Based on density functional theory (DFT) first-principles electronic structure calculations, we try to provide new insights into the unique electronic structures of this uncommon trivalent iridate. We not only successfully reproduce the experimentally observed semiconducting behavior and NM properties, but also reveal the evolutions of the band structure along with the SOC interactions. More interestingly, the in-gap states featured with nearly free electron characteristics are discovered below the conduction bands. Intriguingly, the electronic structure exhibit excellent tunability under mechanical strains, which pave the way for realization band convergence and multiple valleys in $\text{K}_{0.75}\text{Na}_{0.25}\text{IrO}_2$. The present work provides clues to explain the experimentally observed abnormally low activation energy and indicates its potential applications in nanoelectronic and thermoelectric fields.

II. COMPUTATIONAL DETAILS

Employed the projector augmented wave (PAW) method [29,30], first-principles calculations were performed in the framework of DFT with VASP code [31], together with the Perdew-Becke-Ernzerhof (PBE) parameterization of the generalized gradient approximation (GGA) as the exchange-correlation functional [32]. We adopted the rotationally invariant DFT + U method introduced by Liechtenstein *et al.* to consider the correlations effects [33]. The onsite Coulomb interactions U and Hund coupling parameter J_{H} were set to be 2 and 0.2 eV for the Ir atoms, respectively [5,14,15]. Calculations have also taken into account the fully relativistic SOC interactions. The total energy was converged within 10^{-6} eV. The Brillouin zone was sampled using a k -point mesh of $14 \times 14 \times 3$ for the crystallographic unit cell, and the energy cutoff was set to 520 eV.

In order to reveal the preferred occupation positions of the alkali metal ions, first we considered ten configurations in the crystallographic unit cell (schematic models and detailed descriptions were presented in **Figure S1** in SM [34]), which are denoted as NaA, NaB, NaANaB, KA, KB, KAKB, KANaB, KBNaA, KANaA and KBNaB, respectively. Recognized the structural stability and experimental measured positions of the alkali metal ions, we did not consider the configuration that the alkali metal ions only occupy one interlayer position and left another interlayer position empty. Due to the limitation of the unit cell, real compositions of the model are NaIrO_2 , KIrO_2 or $\text{K}_{0.5}\text{Na}_{0.5}\text{IrO}_2$ in these ten configurations. In order to maximize reflect the occupancy of alkali metal

ions in real material of $\text{K}_{0.75}\text{Na}_{0.25}\text{IrO}_2$, we build $2 \times 2 \times 1$ supercells and consider three different occupancy configurations of the alkali metal ions according to the experimentally determined crystallographic structure (as shown in **Figure 2**).

Regarding the layered structure and large interlayer distances along the c -axis, beyond traditional GGA, we took into account the van der Waals (vdW) interactions using different semiempirical dispersion interaction correction methods to relax the crystal structure. However, the vdW corrections play minor role in the lattice constants [see **Figure 3(a)** and **Table S1** in Supplemental Material (SM) [34] for a detailed comparison]. Therefore, we employed the semiempirical dispersion interaction correction methods (DFT-D) with optPBE-vdW functional [35-37] because they nearly predicted identical results.

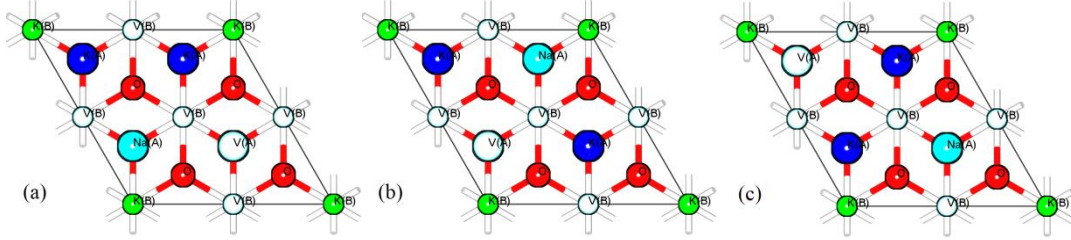


Figure 2 Hypothetical three mixed occupancy configurations of alkali metal ions according to statistical distribution in the interlayer space of $\text{K}_{0.75}\text{Na}_{0.25}\text{IrO}_2$ iridate. The solid line denotes one $2 \times 2 \times 1$ supercell, and there are three K ions and one Na ion in each supercell, corresponding to nominal composition of $\text{K}_{0.75}\text{Na}_{0.25}\text{IrO}_2$. $1/4$ ($2/4$) A positions are occupied by Na (K) ions, whereas only $1/4$ B positions have been occupied by K ions, resulting in 25%/75% vacancies in positions A/B marked as V(A) and V(B).

III. RESULTS AND DISCUSSIONS

Firstly, we pay our attention to the preferential occupation of the alkali metal ions. As shown in **Figure 3(a)**, the in-plane lattice constant a is almost independent on the occupation positions of the alkali metal ions. In contrast, the out-of-plane lattice constant c obviously depends on the occupied positions of the alkali metal ions, which is longer when the alkali metal ions occupy the interlayer position B. As shown in **Figure 1(b)**, these trends can be attributed to the different local geometry of the two interlayer positions, where positions A face to two hollows of the $[\text{IrO}_2]^-$ layers, while positions B face to two surfaces of the IrO_6 octahedra. In addition, owing to the bigger ionic radius of K ions, the lattice constant c is obvious longer when the interlayer positions are only

occupied by K ions. The experimentally observed preferred-occupancy of the alkali metal ions can be further inspected from the energetic point of view. As shown in **Figure 3(b)**, no matter there is one or two types of alkali metal ions, once the alkali metal ions occupy the interlayer positions A, the energies are obvious lower than they occupy the positions B, which are closely related to the hollows of the $[\text{IrO}_2]^-$ layers. Consequently, these two types of alkali metal ions prefer to occupy the interlayer positions A with much lower energy, which are in good agreement with the experimental results, where Na ions almost only occupy the positions A, whereas two third (one third) of K ions occupy positions A (B) [25].

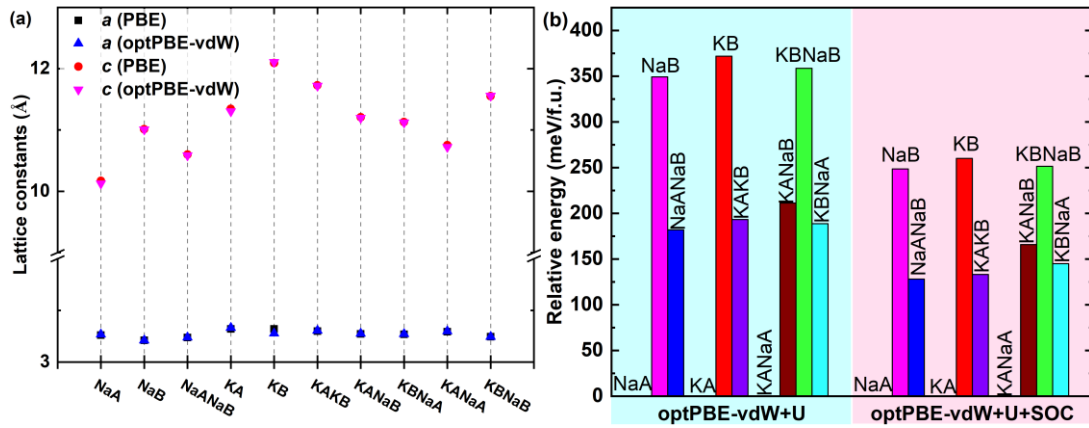


Figure 3 (a) Theoretically calculated lattice constants with PBE or optPBE-vdW functionals and (b) relative energies calculated without or with SOC by optPBE-vdW + U calculations. The energies for the configurations of NaA, KA and KANaA are set as references (zero point).

The original DFT calculations solely consider the interlayer positions are only occupied with K ions by completely neglecting the Na ions, which is inconsistent with the occupancy and composition of the alkali metal ions in real material of $\text{K}_{0.75}\text{Na}_{0.25}\text{IrO}_2$ [25]. Obviously, the resultant electronic structure cannot express the inherent characteristics of $\text{K}_{0.75}\text{Na}_{0.25}\text{IrO}_2$. In this context, we resort to the $2 \times 2 \times 1$ supercells and consider three different occupancy configurations of the alkali metal ions as shown in **Figure 2**. Despite the energy of the second case (**Figure 2(b)**) is significantly lower than the other two cases, the projected band structures show similar characteristics for these three cases (**Figure 4** and **Figures S2-S3** of SM [34], hereafter we just discuss and present the results of $\text{K}_{0.75}\text{Na}_{0.25}\text{IrO}_2$ corresponding to the occupancy configuration of **Figure 2(b)**. The spin polarized calculations are performed to check the basic electronic structure, and the electron correlation interactions together with vdW corrections are considered by optPBE-vdW + U calculations.

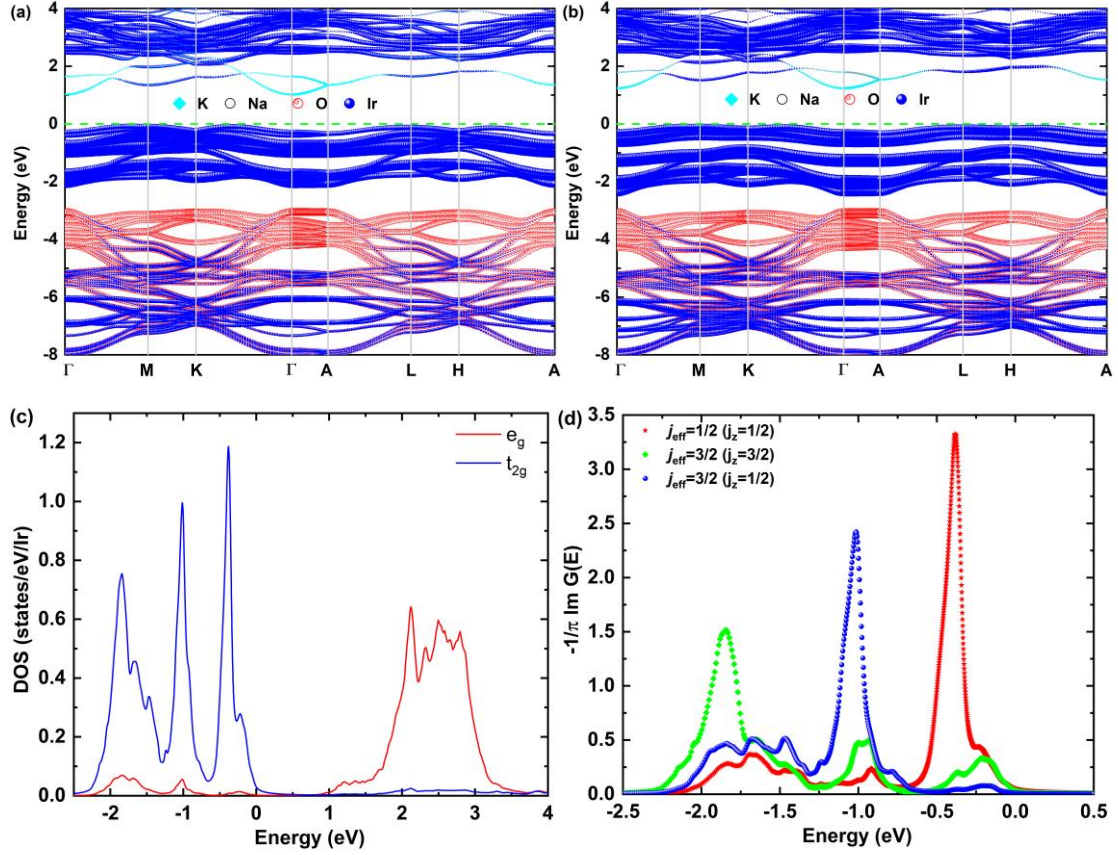


Figure 4 Electronic structure of $K_{0.75}Na_{0.25}IrO_2$ with the mixed occupancy configurations of alkali metal ions as shown in Figure 2(b). (a) and (b) are projected band structures calculated within optPBE-vdW + U without SOC and including SOC, respectively. The bands are projected onto K 4s, Na 3s, O 2p and Ir 5d states, denoted by cyan diamond, black circle, red hollow balls and blue solid balls. The size of the symbols is proportional to the contribution from the corresponding elements. The projection of Ir 5d states onto the t_{2g} , e_g states is presented in (c), and the corresponding projection of the t_{2g} states onto the j_{eff} states is plotted in (d).

As shown in Figure 4, the strong hybridizations between Ir 5d and O 2p states give rise to the Ir 5d bonding bands ranging from -8 to -5 eV [14,15,38-40]. The O 2p states mainly locate above these bonding states, whereas the Ir 5d antibonding states dominantly contribute to the states near E_F . The Ir 5d valence bands are almost flat without dispersion along the Γ -A direction (along the stacking direction of the $[IrO_2]^-$ layers in real space), reflecting weak interlayer interactions in these layered structure iridates [41]. One noteworthy feature is the Ir 5d orbitals have been split into the t_{2g} and e_g states by the octahedral crystal field. Even without onsite Coulomb corrections, the crystal-field splitting is sufficient to account for the insulating nature, the experimentally observed semiconducting behavior has been successfully reproduced. As shown in Figures 4(a) and (c), the

isolated manifold of t_{2g} bands below Fermi level (E_F) are fully occupied, and are distinctly separated away from the fully empty e_g states above E_F by a large crystal-field splitting, resulting in insulating band structures. Due to the two-dimensional connectivity of the IrO_6 octahedra, the bandwidth of the t_{2g} states (about 2 eV) are close to another quasi two-dimensional iridate Sr_2IrO_4 [5,9]. The band structure displays $5d^6$ (t_{2g}^6, e_g^0) electronic configuration with typical NM characteristics, coinciding well with the magnetic measurement results [25]. According to traditional band theory scenario, the layered iridate $\text{K}_{0.75}\text{Na}_{0.25}\text{IrO}_2$ can be classified as band insulator because of even-number of electrons [42,43].

To shed more lights on the underlying role of SOC in the electronic structure, the SOC interactions are included by optPBE-vdW + U + SOC calculations. As shown in **Figure 4(b)**, SOC interactions significantly influence the dispersion of the Ir- t_{2g} states below E_F , but almost have no impact on the dispersion of the Ir- e_g states, the triply degenerate t_{2g} states evolve into $j_{\text{eff}} = 3/2$ quartet and $j_{\text{eff}} = 1/2$ doublet states, which are all fully occupied by the six electrons of the trivalent Ir^{3+} ($5d^6$) ions [1,9]. Because the energy of the $j_{\text{eff}} = 3/2$ states is somewhat lower than that of the $j_{\text{eff}} = 1/2$ states, there are obvious gaps between them [1,7,9]. To get further insight into the nature of the j_{eff} states, we perform non-spin polarized calculations for the NM state of $\text{K}_{0.75}\text{Na}_{0.25}\text{IrO}_2$ using the projection-embedding implementation [44] on top of the WIEN2K package [45]. The projected density of states corresponds to the imaginary part of the Green's function ($-1/\pi \text{Im } G(E)$) [7]. As shown in **Figure 4(d)** and **Figure S4** of SM [34], the projection of the t_{2g} states onto the j_{eff} states is very convenient to identify the $j_{\text{eff}} = 1/2$ and $j_{\text{eff}} = 3/2$ components. Particularly, the $j_{\text{eff}} = 1/2$ states show very high purity, which are distinctly separated from the quartet $j_{\text{eff}} = 3/2$ states. In the strong SOC scenario, the fully occupied j_{eff} states give rise to a NM $J_{\text{eff}} = 0$ characteristics.

Another remarkable feature of the electronic structure of $\text{K}_{0.75}\text{Na}_{0.25}\text{IrO}_2$ is the in-gap states locating at the bottom of the conduction bands. The conduction band minimum (CBM) always located at the high symmetry point Γ , and the states around the high symmetry points Γ and A primarily come from the interlayer alkali metal ions, rather than the Ir 5d states (detailed projected band structures of the CBM are displayed in **Figures 5-6**). Although previous experiment has proposed the existence of in-gap states caused by the extrinsic impurities or lattice defects [25], our band structures demonstrate the in-gap states originate from the intrinsic electronic states of the alkali metal ions. We propose that the insulating $[\text{IrO}_2]^-$ layers act as the blocking layer, while the

alkali metal ions intercalate the interlayer space of the building block of the $[\text{IrO}_2]^-$ layers, and generate the in-gap state. Especially, these in-gap states near Γ point have nearly free electron (NFE) characteristics with parabolic energy dispersions [46]. By fitting the energy band in the vicinity of the Γ point, the effective masses m^* along the Γ -A, Γ -K, and Γ -M directions are estimated to be 0.586, 0.493 and 0.557 m_0 (m_0 is the free-electron mass) for $\text{K}_{0.75}\text{Na}_{0.25}\text{IrO}_2$ calculated by optPBE-vdW + U without SOC. Including SOC interactions, the corresponding effective masses m^* are 0.639, 0.513 and 0.603 m_0 , respectively. The deviations of effective masses m^* from free-electron mass m_0 widely exist in other NFE systems. For example, the m^* of two NFE states in the bulk gap of silicon are 0.404 and 0.314 m_0 [47], and the m^* of NFE states in carbon and boron nitride nanotubes are 1.2 m_0 [48]. The in-gap states and NFE characteristics provide clues to the experimentally observed abnormal low activation energy of $\text{K}_{0.75}\text{Na}_{0.25}\text{IrO}_2$.

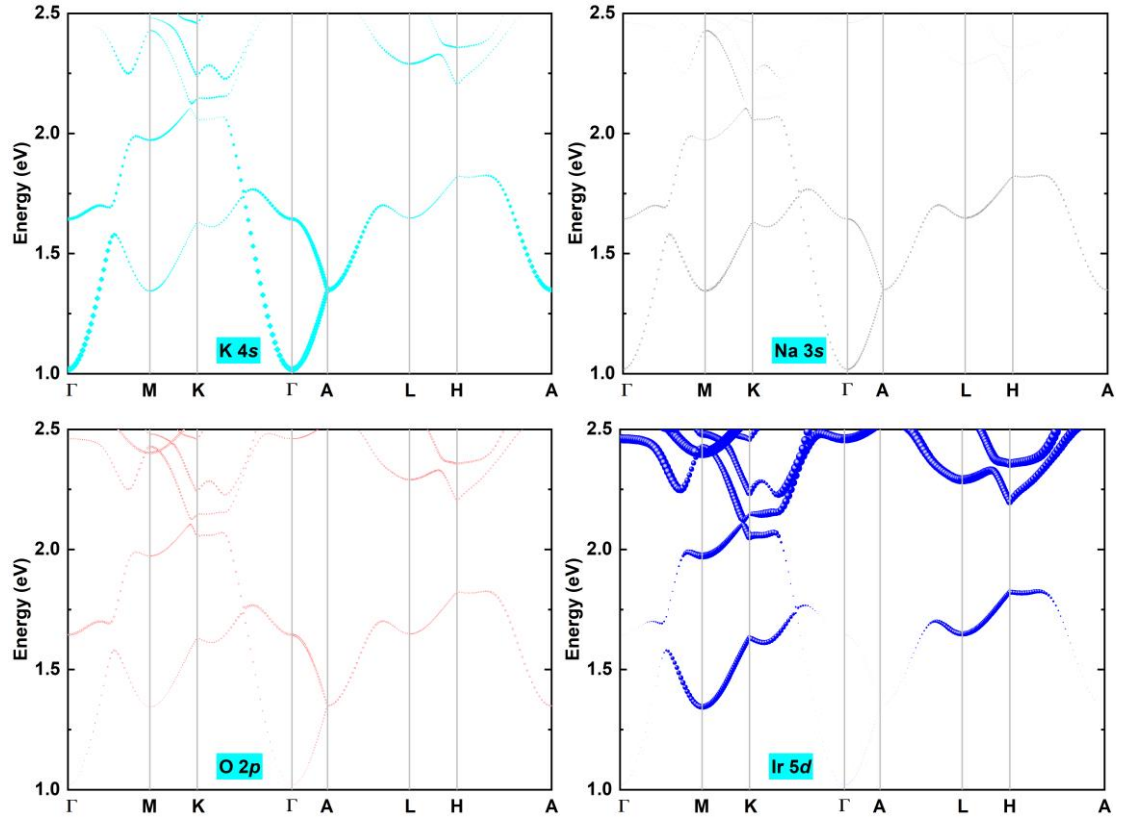


Figure 5 Projected CBM of $\text{K}_{0.75}\text{Na}_{0.25}\text{IrO}_2$ calculated within optPBE-vdW + U without SOC, which are projected onto K 4s, Na 3s, O 2p and Ir 5d states, denoted by cyan diamond, black circle, red hollow balls and blue solid balls. The size of the symbols is proportional to the contribution from the corresponding elements.

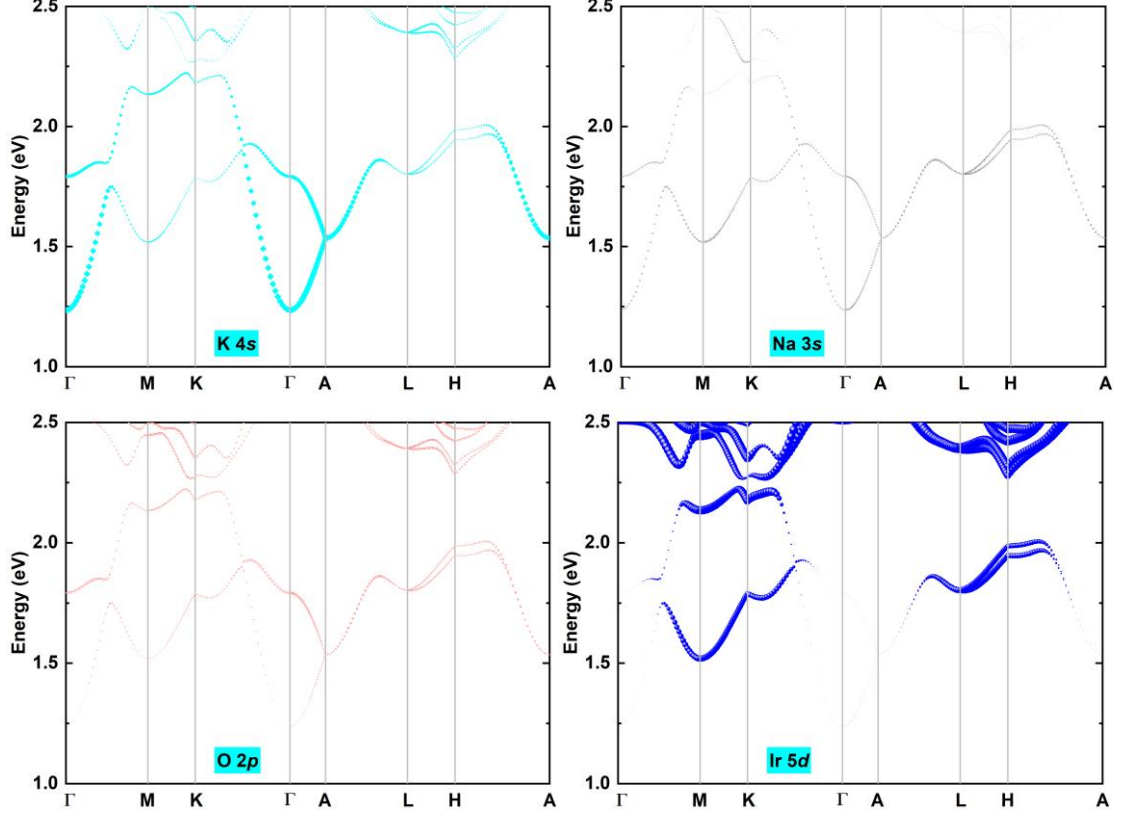


Figure 6 Projected CBM of $\text{K}_{0.75}\text{Na}_{0.25}\text{IrO}_2$ calculated within optPBE-vdW + U with SOC, which are projected onto K 4s, Na 3s, O 2p and Ir 5d states, denoted by cyan diamond, black circle, red hollow balls and blue solid balls. The size of the symbols is proportional to the contribution from the corresponding elements.

As shown in **Figure 7**, we can gain further insight into the nature of the NFE states by looking at the composition of the charge densities at Γ point for the CBM. The charge densities are delocalized, where the charge densities are not localized around alkali metal ions but are distributed within the whole interstitial region between two $[\text{IrO}_2]^-$ layers. The NFE states have been proposed as ideal electron transport channels without nuclear scattering [49]. They are originally proposed to exist in graphite and alkali graphite intercalation compounds, displaying free-electron character parallel to the graphitic layers [50]. NFE states have been widely discovered in other carbon-based materials (such as graphene, nanotubes, and fullerenes [48,51-53]) as well as two-dimensional transition metal carbides and nitrides (MXenes [46], hexagonal boron nitride [41], and Ca_2N monolayer [49]). The NFE states are usually unoccupied and located at high energy region, and unsuitable to be used as transport channel [46]. Fortunately, the NFE states in the title iridate $\text{K}_{0.75}\text{Na}_{0.25}\text{IrO}_2$ are located at the CBM, which renders them more accessible for electron transport

or other applications than other known two-dimensional systems [46,49].

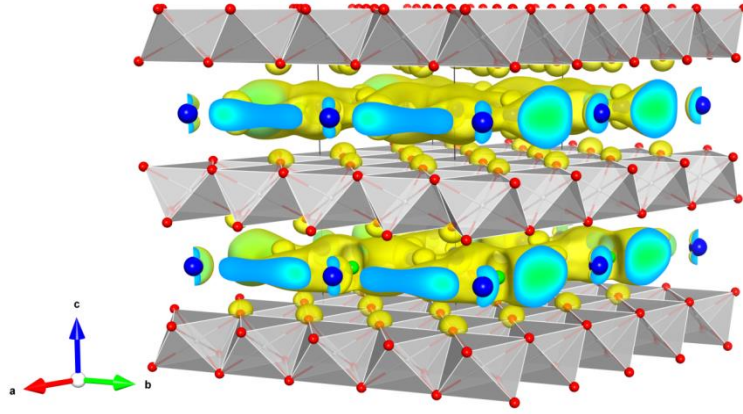


Figure 7 Charge density maps (isosurface value is $0.008 \text{ e}/\text{\AA}^3$) of the CBM state at the Γ point for the $\text{K}_{0.75}\text{Na}_{0.25}\text{IrO}_2$ calculated within optPBE-vdW + U .

In addition to the fascinating in-gap states, the electronic structure of $\text{K}_{0.75}\text{Na}_{0.25}\text{IrO}_2$ also exhibits the attractive band-convergence characteristics. As shown in the zoom-in view of the band structure around Fermi level (**Figure S5** of SM [34]), the conduction bands of $\text{K}_{0.75}\text{Na}_{0.25}\text{IrO}_2$ possess two other local band-minima locating at the M point and A point beyond the global CBM of Γ point, whereas the valence band maximum (VBM) locates along the Γ -M direction accompanying with three other local extrema along the Γ -K, L-A and H-A directions, respectively. The bands are regarded as effectively converged when the band extrema of the multiple bands have no or little difference in energy, which leads to the increasing of the valley degeneracy and enhancement of electrical conductivity [54,55]. The band convergence of multi-valley conduction bands and multi-peak valence bands has been demonstrated as an effective strategy in improvement of the electrical conductivity and quality factor of thermoelectric materials [56]. In this sense, $\text{K}_{0.75}\text{Na}_{0.25}\text{IrO}_2$ could be a promising candidate of thermoelectric material with high electrical conductivity provided that the energy differences between the local band-extrema and CBM/VBM are within two times of the thermal energy at room temperature ($2k_B T$, where k_B is the Boltzmann constant).

The uniaxial strain is an adequate means to manipulate the band convergence and the number of the degenerated band valleys [57]. We simulate the mechanical strain by changing the lattice constant c to probe the strain effect on the electronic structure of the $\text{K}_{0.75}\text{Na}_{0.25}\text{IrO}_2$. The relationship between mechanical strain and lattice constant can be expressed as: $\varepsilon = (c - c_0)/c_0$, where c and c_0

are the lattice constant c for the strained and unstrained cell, respectively. A negative (positive) value of ε is defined as compressive (tensile) strain, which are realized by compressing (stretching) the crystal lattice along the c axis direction. In the strain-free state, the $\text{K}_{0.75}\text{Na}_{0.25}\text{IrO}_2$ is an indirect bandgap semiconductor. The evolution of the band structure along with the applied strain is summarized in [Figure S6](#) of SM [34]. As shown in [Figure 8\(a\)](#), the CBM, VBM and band gap linearly vary with the applied strain. The CBM and the VBM increase upon the increasing compressive strain ($\varepsilon < 0$), which decrease along with the tensile strain ($\varepsilon > 0$). When subjected to tensile stress along c -axis, except for leading to band gap shrinkage, the tensile strain plays minor impact on the dispersion of the conduction bands and the in-gap states (detailed band structures are shown in [Figure S7](#) of SM [34]). By contrast, as the compressive strain increases, the conduction bands near the Γ point move up and the bands near the M point move down, eventually causing the CBM to be converted from the s states of alkali metal ions to Ir-5d states (detailed band structures are shown in [Figure S8](#) of SM [34]), and resulting in band gap enlargement.

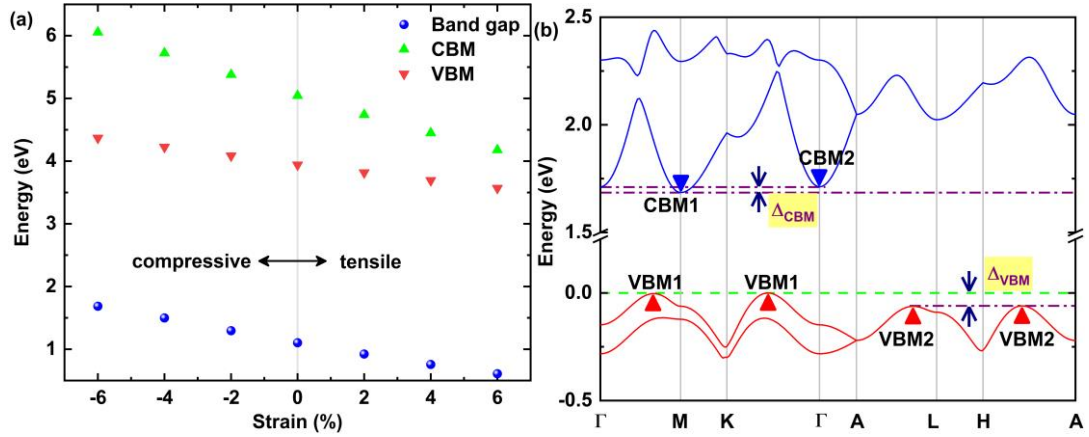


Figure 8 (a) The evolutions of the CBM, VBM, and band gap along with the applied strain calculated with optPBE-vdW + U . (b) A zoom-in view of band convergence and multiple valleys achieved by 6% compressive strain.

As shown in [Figure 8\(b\)](#), the local valence-band extremum along the Γ -K direction is elevated and becomes degenerate with the VBM along the Γ -M direction when the compressive strain increases up to 6% (which are denoted as VBM1). In addition, the local valence-band extremum along the H-A direction becomes degenerate with the extremum along the L-A direction (which are denoted as VBM2). The energy difference between VBM1 and VBM2 is about 62 meV, which is close to $2k_{\text{B}}T$ (~ 52 meV). More interestingly, the locating of the global CBM has changed from the

Γ point to M point along with the compression, which leads to two conduction band valleys. The energy difference between these two valleys of CBM1 and CBM2 is only 25 meV, which is far less than $2k_B T$. According to the evolution tendency of band structure under mechanical strain, the concomitant variation of the band edge may lead to completely degenerate CBM. The convergence of the band extrema has led to prominent increase of the valley degeneracy, which are highly likely to make contribution to the electrical conductivity and thermoelectric quality factor of $K_{0.75}Na_{0.25}IrO_2$ [54-57]. The above theoretical results indicate that the electronic structure of $K_{0.75}Na_{0.25}IrO_2$ could be effectively modulated by strain, and strain-induced band convergence could be an effective method to tune the thermoelectric performance of $K_{0.75}Na_{0.25}IrO_2$.

IV. CONCLUSIONS

In summary, the first-principles DFT calculations and simulations have been performed to explore the intrinsic electronic structure of the layered iridates $K_{0.75}Na_{0.25}IrO_2$. The preferred-occupied positions of the alkali metal ions are theoretically reproduced from an energetic viewpoint. The crystal-field splitting is sufficient to rationalize the insulating nature, and the layered iridates $K_{0.75}Na_{0.25}IrO_2$ can be classified as band insulator. The SOC interactions play critical role in the band structure, resulting in NM $J_{\text{eff}} = 0$ states for the trivalent Ir^{3+} ($5d^6$) ions. Intriguingly, the electronic structure calculations reveal the presence of in-gap states located below the conduction bands, which are responsible for the experimentally observed abnormal low activation energy in $K_{0.75}Na_{0.25}IrO_2$. In addition, the in-gap states with parabolic energy dispersions exhibit NFE characteristics, which primarily come from the inherent alkali metal ions rather than the impurities or lattice defects. Furthermore, the band structure and band edge exhibit excellent tunability under mechanical strains. Particularly, the VBM and CBM are effectively converged by the uniaxial compression, which gives rise to significant increase of the valley degeneracy and will significantly contribute to the electrical conductivity of $K_{0.75}Na_{0.25}IrO_2$. Present theoretical results provide new insights into the unique electronic structures of the layered structure iridates, which implies $K_{0.75}Na_{0.25}IrO_2$ is a potential material for future nanoelectronic and thermoelectric applications, waiting for further experimental verifications.

ACKNOWLEDGMENTS

We gratefully acknowledge the financial support by the National Natural Science Foundation of China (No. 11864008, 12264011), Guangxi Natural Science Foundation (No.

2018GXNSFAA138185 and AD19110081). The computational work in this research was carried out at Shanxi Supercomputing Center, and the calculations were performed on TianHe-2.

Reference

- 1 Rau, Jeffrey G., Eric Kin-Ho Lee, and Hae-Young Kee. "Spin-orbit physics giving rise to novel phases in correlated systems: Iridates and related materials." *Annual Review of Condensed Matter Physics* **7** (2016): 195-221.
- 2 Witczak-Krempa, William, et al. "Correlated quantum phenomena in the strong spin-orbit regime." *Annual Review of Condensed Matter Physics* **5** (2014): 57-82.
- 3 Cao, Gang, and Pedro Schlottmann. "The challenge of spin-orbit-tuned ground states in iridates: a key issues review." *Reports on Progress in Physics* **81** (2018): 042502.
- 4 Pesin, Dmytro, and Leon Balents. "Mott physics and band topology in materials with strong spin-orbit interaction." *Nature Physics* **6** (2010): 376.
- 5 Moon, S. J., et al. "Dimensionality-Controlled Insulator-Metal Transition and Correlated Metallic State in 5d Transition Metal Oxides $\text{Sr}_{n+1}\text{Ir}_n\text{O}_{3n+1}$ ($n=1, 2$, and ∞)." *Physical Review Letters* **101** (2008): 226402.
- 6 Kawasaki, Jason K., et al. "Evolution of electronic correlations across the rutile, perovskite, and Ruddelsden-Popper iridates with octahedral connectivity." *Physical Review B* **94** (2016): 121104.
- 7 Ming, Xing, et al. "Spin-orbit coupling driven insulating state in hexagonal iridates Sr_3MIrO_6 ($\text{M}=\text{Sr}, \text{Na}, \text{Li}$)." *Physical Review B* **98** (2018): 245123.
- 8 Martins, Cyril, Markus Aichhorn, and Silke Biermann. "Coulomb correlations in 4d and 5d oxides from first principles—or how spin-orbit materials choose their effective orbital degeneracies." *Journal of Physics: Condensed Matter* **29** (2017): 263001.
- 9 Kim, B. J., et al. "Novel $J_{\text{eff}}=1/2$ Mott state induced by relativistic spin-orbit coupling in Sr_2IrO_4 ." *Physical Review Letters* **101** (2008): 076402.
- 10 Kim, B. J., et al. "Phase-sensitive observation of a spin-orbital Mott state in Sr_2IrO_4 ." *Science* **323** (2009): 1329-1332.
- 11 Wan, Xiangang, et al. "Topological semimetal and Fermi-arc surface states in the electronic structure of pyrochlore iridates." *Physical Review B* **83** (2011): 205101.
- 12 Wang, Runzhi, Ara Go, and Andrew J. Millis. "Electron interactions, spin-orbit coupling, and intersite correlations in pyrochlore iridates." *Physical Review B* **95** (2017): 045133.
- 13 Chen, Yige, Yuan-Ming Lu, and Hae-Young Kee. "Topological crystalline metal in orthorhombic perovskite iridates." *Nature Communications* **6** (2015): 6593.
- 14 Ming, Xing, et al. "Role of square planar coordination in the magnetic properties of Na_4IrO_4 ." *Physical Review B* **96** (2017): 205158.
- 15 Wang, Di, et al. "First-principles study of the giant magnetic anisotropy energy in bulk Na_4IrO_4 ." *Physical Review B* **96** (2017): 205159.

- 16 Yan, Y. J., et al. "Electron-doped Sr_2IrO_4 : an analogue of hole-doped cuprate superconductors demonstrated by scanning tunneling microscopy." *Physical Review X* **5** (2015): 041018.
- 17 Kim, Yeong Kwan, et al. "Fermi arcs in a doped pseudospin-1/2 Heisenberg antiferromagnet." *Science* **345** (2014): 187-190.
- 18 Zhao, L., et al. "Evidence of an odd-parity hidden order in a spin-orbit coupled correlated iridate." *Nature Physics* **12** (2016): 32.
- 19 Kim, Yeong Kwan, et al. "Observation of a d-wave gap in electron-doped Sr_2IrO_4 ." *Nature Physics* **12** (2016): 37.
- 20 Okamoto, Yoshihiko, et al. "Spin-liquid state in the $S = 1/2$ hyperkagome antiferromagnet $\text{Na}_4\text{Ir}_3\text{O}_8$." *Physical Review Letters* **99** (2007): 137207.
- 21 Machida, Yo, et al. "Time-reversal symmetry breaking and spontaneous Hall effect without magnetic dipole order." *Nature* **463** (2010): 210.
- 22 Matar, Samir F., and Jean Etourneau. " $(\text{CaO})_n\text{IrO}_2$ ($n = 1, 2, 4$) family: Chemical scissors effects of CaO on structural characteristics correlated to physical properties. Ab initio study." *Journal of Solid State Chemistry* **255** (2017): 82-88.
- 23 Groenendijk, D. J., et al. "Spin-orbit semimetal SrIrO_3 in the two-dimensional limit." *Physical Review Letters* **119** (2017): 256403.
- 24 Nie, Yuefeng F., et al. "Interplay of spin-orbit interactions, dimensionality, and octahedral rotations in semimetallic SrIrO_3 ." *Physical Review Letters* **114** (2015): 016401.
- 25 Weber, Daniel, et al. "Trivalent iridium oxides: layered triangular lattice iridate $\text{K}_{0.75}\text{Na}_{0.25}\text{IrO}_2$ and oxyhydroxide IrOOH ." *Chemistry of Materials* **29** (2017): 8338-8345.
- 26 Momma, Koichi, and Fujio Izumi. "VESTA3 for three-dimensional visualization of crystal, volumetric and morphology data." *Journal of Applied Crystallography* **44** (2011): 1272-1276.
- 27 Curtarolo, Stefano, et al. "AFLOW: an automatic framework for high-throughput materials discovery." *Computational Materials Science* **58** (2012): 218-226.
- 28 Setyawan, Wahyu, and Stefano Curtarolo. "High-throughput electronic band structure calculations: Challenges and tools." *Computational Materials Science* **49** (2010): 299-312.
- 29 Blöchl, Peter E. "Projector augmented-wave method." *Physical Review B* **50** (1994): 17953.
- 30 Kresse, Georg, and D. Joubert. "From ultrasoft pseudopotentials to the projector augmented-wave method." *Physical Review B* **59** (1999): 1758.
- 31 Kresse, Georg, and Jürgen Furthmüller. "Efficient iterative schemes for ab initio total-energy calculations using a plane-wave basis set." *Physical Review B* **54** (1996): 11169.
- 32 Perdew, John P., et al. "Restoring the density-gradient expansion for exchange in solids and surfaces." *Physical Review Letters* **100** (2008): 136406.
- 33 Liechtenstein, A. I., V. I. Anisimov, and J. Zaanen. "Density-functional theory and strong interactions: Orbital ordering in Mott-Hubbard insulators." *Physical Review B* **52** (1995): R5467.
- 34 [Supplemental Material](#)

- 35 Dion, Max, et al. "Van der Waals density functional for general geometries." *Physical Review Letters* **92** (2004): 246401.
- 36 Klimeš, Jiří, David R. Bowler, and Angelos Michaelides. "Chemical accuracy for the van der Waals density functional." *Journal of Physics: Condensed Matter* **22** (2009): 022201.
- 37 Klimeš, Jiří, David R. Bowler, and Angelos Michaelides. "Van der Waals density functionals applied to solids." *Physical Review B* **83** (2011): 195131.
- 38 Ou, Xuedong, and Hua Wu. "Impact of spin-orbit coupling on the magnetism of Sr_3MIrO_6 ($\text{M} = \text{Ni}, \text{Co}$)." *Scientific Reports* **4** (2014): 4609.
- 39 Bhowal, Sayantika, and I. Dasgupta. "Covalency and spin-orbit coupling driven magnetism in the double-perovskite iridates Sr_2MIrO_6 ($\text{M} = \text{Ca}, \text{Mg}$)." *Physical Review B* **97** (2018): 024406.
- 40 Paramakanti, Arun, et al. "Spin-orbit coupled systems in the atomic limit: rhenates, osmates, iridates." *Physical Review B* **97** (2018): 235119.
- 41 Blase, Xavier, et al. "Quasiparticle band structure of bulk hexagonal boron nitride and related systems." *Physical Review B* **51** (1995): 6868.
- 42 Chen, Gang, and Leon Balents. "Spin-orbit coupling in d^2 ordered double perovskites." *Physical Review B* **84** (2011): 094420.
- 43 Meetei, O. Nganba, et al. "Novel magnetic state in d^4 Mott insulators." *Physical Review B* **91** (2015): 054412.
- 44 K. Haule, C. Yee, and K. Kim. "Dynamical mean-field theory within the full-potential methods: Electronic structure of CeIrIn_5 , CeCoIn_5 , and CeRhIn_5 ." *Physical Review B* **81** (2010): 195107.
- 45 <http://www.wien2k.at>.
- 46 Khazaei, Mohammad, et al. "Nearly free electron states in MXenes." *Physical Review B* **93** (2016): 205125.
- 47 Gou, Jian, et al. "Scanning tunneling microscopy investigations of unoccupied surface states in two-dimensional semiconducting $\beta\text{-}\sqrt{3}\times\sqrt{3}\text{-Bi/Si}$ (111) surface." *Physical Chemistry Chemical Physics* **20** (2018): 20188-20193.
- 48 Hu, Shuanglin, et al. "Nearly free electron superatom states of carbon and boron nitride nanotubes." *Nano Letters* **10** (2010): 4830-4838.
- 49 Zhao, Songtao, Zhenyu Li, and Jinlong Yang. "Obtaining two-dimensional electron gas in free space without resorting to electron doping: an electride based design." *Journal of the American Chemical Society* **136** (2014): 13313-13318.
- 50 Posternak, M., et al. "Prediction of electronic interlayer states in graphite and reinterpretation of alkali bands in graphite intercalation compounds." *Physical Review Letters* **50** (1983): 761.
- 51 Posternak, M., et al. "Prediction of electronic surface states in layered materials: graphite." *Physical Review Letters* **52** (1984): 863.
- 52 Okada, Susumu, Atsushi Oshiyama, and Susumu Saito. "Nearly free electron states in carbon nanotube bundles." *Physical Review B* **62** (2000): 7634.

- 53 Yang, Y. E., Y. Xiao, and X. H. Yan. "Charge distribution of Lithium-doped graphane/graphene hybrid system: Role of nearly-free electronic states." *Solid State Communications* **229** (2016): 43-48.
- 54 Pei, Y., Shi, X., LaLonde, A. et al. "Convergence of electronic bands for high performance bulk thermoelectrics." *Nature* **473** (2011): 66–69.
- 55 Heremans, J. et al. "Enhancement of thermoelectric efficiency in PbTe by distortion of the electronic density of states." *Science* **321** (2008): 554–557.
- 56 Tang, Y., Gibbs, Z., Agapito, L. et al. "Convergence of multi-valley bands as the electronic origin of high thermoelectric performance in CoSb₃ skutterudites." *Nature Materials* **14** (2015): 1223–1228.
- 57 Lv, H. Y., Lu, W. J., Shao, D. F. and Sun, Y. P. "Enhanced thermoelectric performance of phosphorene by strain-induced band convergence." *Physical Review B* **90** (2014): 085433.